This is the accepted manuscript made available via CHORUS. The article has been published as:

Crystal field levels and magnetic anisotropy in the kagome compounds Nd_{3}Sb_{3}Mg_{2}O_{14}, Nd_{3}Sb_{3}Zn_{2}O_{14}, and Pr_{3}Sb_{3}Mg_{2}O_{14}

A. Scheie, M. Sanders, J. Krizan, A. D. Christianson, V. O. Garlea, R. J. Cava, and C. Broholm

Phys. Rev. B **98**, 134401 — Published 1 October 2018

DOI: 10.1103/PhysRevB.98.134401

Crystal Field Levels and Magnetic Anisotropy in the Kagome Compounds $Nd_3Sb_3Mg_2O_{14}$, $Nd_3Sb_3Zn_2O_{14}$, and $Pr_3Sb_3Mg_2O_{14}$

A. Scheie,[1] M. Sanders,[2] J. Krizan,[2] A. D. Christianson,[3,4] V. O. Garlea,[3] R.J. Cava,[2] and C. Broholm[1,5,6]

[1] *Institute for Quantum Matter and Department of Physics and Astronomy, Johns Hopkins University, Baltimore, MD 21218*

[2] *Department of Chemistry, Princeton University, Princeton, NJ 08544*

[3] *Neutron Scattering Division, Oak Ridge National Laboratory, Oak Ridge, Tennessee 37831, USA*

[4] *Materials Science & Technology Division, Oak Ridge National Laboratory, Oak Ridge, TN 37831, USA*

[5] *NIST Center for Neutron Research, National Institute of Standards and Technology, Gaithersburg, MD 20899*

[6] *Department of Materials Science and Engineering, Johns Hopkins University, Baltimore, MD 21218*

(Dated: September 14, 2018)

We report the crystal field levels of several newly-discovered rare-earth kagome compounds: $Nd_3Sb_3Mg_2O_{14}$, $Nd_3Sb_3Zn_2O_{14}$, and $Pr_3Sb_3Mg_2O_{14}$. We determine the CEF Hamiltonian by fitting to neutron scattering data using a point-charge Hamiltonian as an intermediate fitting step. The fitted Hamiltonians accurately reproduce bulk susceptibility measurements, and the results indicate easy-axis ground state doublets for $Nd_3Sb_3Mg_2O_{14}$ and $Nd_3Sb_3Zn_2O_{14}$, and a singlet ground state for $Pr_3Sb_3Mg_2O_{14}$. These results provide the groundwork for future investigations of these compounds and a template for CEF analysis of other low-symmetry materials.

I. INTRODUCTION

The kagome lattice of corner-sharing triangles is the basis for multiple distinct forms of frustrated magnetism with unique physical properties. Magnetic kagome lattices are believed to host spin-liquid phases[1–4], non-trivial transport properties[5], and topologically protected phases[6]. Experimental realizations of these models present important opportunities to explore new states of matter.

Recently, a new family of kagome compounds with magnetic rare earth ions $RE_3Sb_3A_2O_{14}$ (RE = rare earth, A = Mg, Zn) was discovered[7–9]. Basic materials characterization has been carried out on the entire family[7–10], and neutron diffraction has revealed the low temperature magnetic structure of $Nd_3Sb_3Mg_2O_{14}$[11] and $Dy_3Sb_3Mg_2O_{14}$[12]. μSR data for $Tb_3Sb_3Zn_2O_{14}$ were interpreted as indicative of a spin-liquid ground state[13].

The rare earth ions in these materials are strongly influenced by the electrostatic environment they occupy. It determines to what extent and how the $2J+1$ fold spin-orbital degeneracy of the rare earth ion is lifted[14]. Clearly this has major impacts on the nature of the potentially frustrated magnetism. Fortunately the crystal electric field (CEF) level scheme can be accurately determined using inelastic neutron scattering and it is to this task that we have devoted ourselves in this paper. Specifically, we report the crystal field Hamiltonians of the insulating compounds $Nd_3Sb_3Mg_2O_{14}$, $Nd_3Sb_3Zn_2O_{14}$, and $Pr_3Sb_3Mg_2O_{14}$ deduced from crystal field excitations observed with neutron scattering. The complexity of the CEF Hamiltonian is determined by the point group symmetry of the ion: high symmetry means few CEF parameters, low symmetry means many CEF parameters. The ligand environment for $RE_3Sb_3A_2O_{14}$ (RE = rare earth, A = Mg, Zn) has a very low symmetry oxygen environment of $2/m$ symmetry (see Fig. 1), leading to 15 allowed CEF parameters in the Hamiltonian. Such a model is very difficult to uniquely establish, but—by using a point-charge approximation to obtain a first approximation—reliable fits to neutron scattering data are possible. The techniques outlined here provide a template for analyzing the rest of this family of Kagome compounds and indeed they should be useful for analyzing the crystal field level scheme when as here the symmetries involved are low.

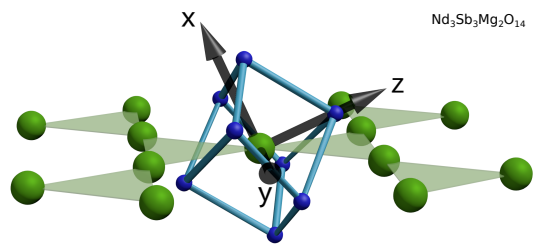

Figure 1. Distorted scalenohedron ligand environment of Nd in $Nd_3Sb_3Mg_2O_{14}$. The axes at the center show the local axes used to model the crystal fields. $Nd_3Sb_3Zn_2O_{14}$ and $Pr_3Sb_3Mg_2O_{14}$ have the same symmetry, but with slightly different oxygen locations.

II. EXPERIMENTAL METHODS

We performed neutron scattering experiments on 5g of $Nd_3Sb_3Mg_2O_{14}$, 5g $Nd_3Sb_3Zn_2O_{14}$, and 5g $Pr_3Sb_3Mg_2O_{14}$ (all loose powders) on the ARCS spectrometer at the SNS at ORNL. For every compound, we collected data at incident energies $E_i = 150$ meV, $E_i = 80$meV, and $E_i = 40$meV; at temperatures $T = 6$K, $T = 100$ K, and $T = 200$ K for every E_i (a total of

nine data sets), measuring for two hours at each setting. We also acquired data for a 5g nonmagnetic analogue $La_3Sb_3Mg_2O_{14}$ to serve as a background. This allows us to subtract the phonon contribution from the data for the magnetic compounds (see supplemental materials[26] for details about the background subtraction).

The full background-subtracted data set for $Nd_3Sb_3Mg_2O_{14}$ is shown in Fig. 2. The crystal field excitations are clearly visible because the corresponding intensity decreases with Q as a result of the electronic form factor. As Nd^{3+} is a $J = 9/2$ Kramers ion, we expect to see $10/2 = 5$ CEF levels, and thus four CEF transition energies from the ground state. This is indeed what we observe in the neutron data: in the 6 K data, four transitions are visible at 23 meV, 36 meV, 43 meV, and 111 meV. At higher temperatures, the existing peaks broaden in ΔE due to shorter excited-state lifetimes, and additional weak peaks appear corresponding to transitions between thermally populated excited levels.

An abbreviated (6 K only) data set for $Nd_3Sb_3Zn_2O_{14}$ is shown in Fig. 3. These data are nearly identical to the $Nd_3Sb_3Mg_2O_{14}$ data in Fig. 2, with four transitions from a $J = 9/2$ Kramers ion, but with transition energies at 18 meV, 32 meV, 40 meV, and 109 meV. Such differences indicate slight modifications in the ligand environment experienced by the rare earth ion.

An abbreviated (6 K only) data set for $Pr_3Sb_3Mg_2O_{14}$ is shown in Fig. 4. Pr^{3+} is a non-Kramers ion with $J = 4$, which means that singlet states are possible when the point group symmetry is sufficiently low so the number of transitions observed is greater. Five transitions are clearly distinguishable at 6 K, with more being too weak to distinguish in the figure.

III. COMPUTATIONAL METHODS

Using the inelastic neutron scattering data, we were able to infer a crystal field model for each of the compounds that can account for their anisotropic magnetic properties for temperatures above the inter-site interaction scale (1 K). The fits were carried out using the PyCrystalField software package[15]. The analysis is based on the following CEF Hamiltonian

$$\mathcal{H}_{CEF} = \sum_{n,m} B_n^m O_n^m. \tag{1}$$

Here O_n^m are the Stevens Operators[16,17] and B_n^m are multiplicative factors called CEF parameters that parametrize the effects of the ligand environment on the rare earth ion. This formalism is convenient when the ligand environment has high symmetry, leaving only a handful of CEF parameters to be fit[17]. Unfortunately, a direct fit to the data for $Nd_3Sb_3Mg_2O_{14}$ is not feasible: fitting 15 parameters to eight observables (four transition energies and four neutron intensities). To get around this, we begin with a constrained fit based on an electrostatic point-charge model of the ligand environment. Specifically, the point charge $\mathcal{H}_{CEF}$ is based on a Taylor expansion of the electrostatic field at the rare earth site generated by the coordinating atoms treated as point charges[17,18]. This approximation is valid for insulating compounds, which $Nd_3Sb_3Mg_2O_{14}$, $Nd_3Sb_3Zn_2O_{14}$, and $Pr_3Sb_3Mg_2O_{14}$ are.

As is shown in Fig. 1, we chose our axes such that the two-fold rotation symmetry about the y axis, which leads to 15 allowed CEF parameters in the Hamiltonian. The placement of the rotation axis in the xy plane ensures that all imaginary CEF terms are zero[19].

Following the method outlined by Hutchings[17], the CEF parameters B_n^m are given by

$$B_n^m = -\gamma_{nm} q \; C_{nm} \langle r^n \rangle \, \theta_n. \tag{2}$$

Here γ_{nm} is a term calculated from the ligand environment expressed in terms of tesseral harmonics, q is the charge of the central ion (in units of $|e|$), C_{nm} are normalization factors of the tesseral harmonics[17], $\langle r^n \rangle$ is the expectation value of the radial wavefunction for the rare earth ion[20], and θ_n are multiplicative factors from expressing the electrostatic potential in terms of Stevens Operators in the J basis[16].

The neutron cross section for a single CEF transition in a powder sample is

$$\frac{d^2\sigma}{d\Omega d\omega} = N(\gamma r_0)^2 \frac{k'}{k} f^2(\mathbf{Q}) e^{-2W(\mathbf{Q})} \\ p_n |\langle \Gamma_m | \hat{J}_\perp | \Gamma_n \rangle|^2 \delta(\hbar\omega + E_n - E_m) \tag{3}$$

[21], where N is the number of ions, $\gamma = 1.832 \times 10^8 \mathrm{s}^{-1}\mathrm{T}^{-1}$ is the gyromagnetic ratio of the neutron, $r_0 = 2.818 \times 10^{-15}$m is the classical electron radius, k and k' are the incoming and outgoing neutron wavevectors, $f(\mathbf{Q})$ is the form factor, $e^{-2W(\mathbf{Q})}$ is the Debye Waller factor, $p_n = e^{-\beta E_n} / \sum_i e^{-\beta E_i}$ is the Boltzmann weight, and $|\langle \Gamma_m | \hat{J}_\perp | \Gamma_n \rangle|^2 = \frac{2}{3} \sum_\alpha |\langle \Gamma_m | \hat{J}_\alpha | \Gamma_n \rangle|^2$ is computed from the inner product of total angular momentum J_α with the CEF eigenstates $|\Gamma_n\rangle$. Using this equation, one can calculate the neutron spectrum of a given CEF Hamiltonian at a given temperature. In reality, the delta function $\delta(\hbar\omega + E_n - E_m)$ is replaced with a finite width peak due to the limited energy resolution of the instrument, dispersion, and/or the finite lifetime of the excitation. The resolution was approximated with a Gaussian profile, while finite lifetimes give Lorentzian profiles. We approximated the convolution of these with a Voigt profile for computational efficiency. The energy transfer depedendent resolution width was calculated as described in ref.[22] with sample width dL_3 defined so the calculated Full Width at Half Maximum (FWHM) of the elastic line matched the measured FWHM. The finite lifetime Lorentzian width was a single temperature dependent fitting parameter shared by all transitions.

Multiple constant-Q spectra were fitted simultaneously computing the Q-dependent scattering using the calcu-

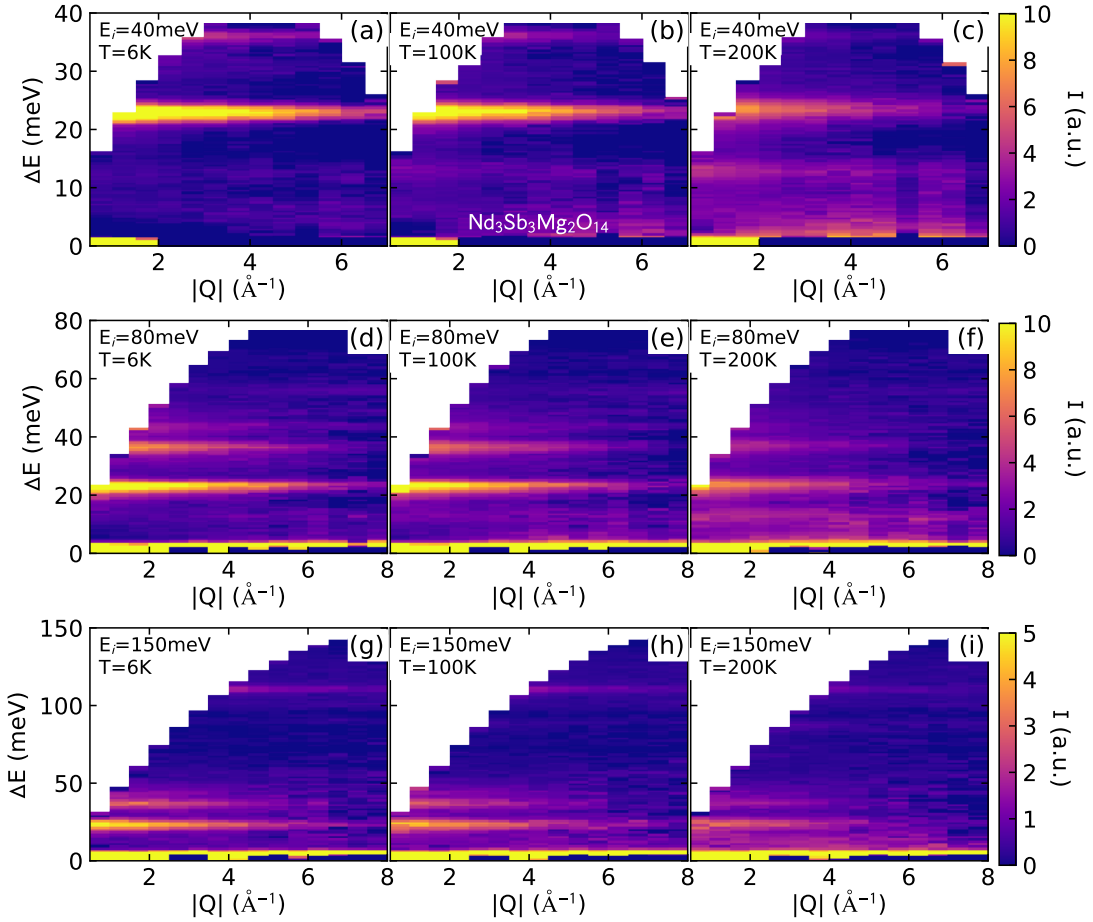

Figure 2. Inelastic neutron scattering from $Nd_3Sb_3Mg_2O_{14}$, taken at E_i =150 meV, 80 meV, and 40 meV and T =6 K, 100 K, and 200 K. Scattering from nonmagnetic $La_3Sb_3Mg_2O_{14}$ was scaled and subtracted to eliminate phonon scattering. The CEF excitations are clearly visible and become broadened as temperature increases.

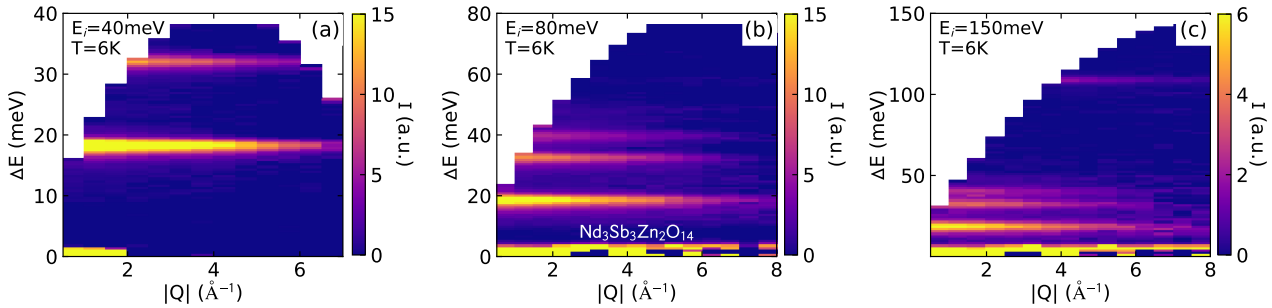

Figure 3. Inelastic neutron scattering from $Nd_3Sb_3Zn_2O_{14}$, taken at E_i =150 meV, 80 meV, and 40 meV and T =6 K (100 K and 200 K data are not shown). Scaled $La_3Sb_3Mg_2O_{14}$ scattering was subtracted. Note the similarity of the patterns to Fig. 2.

lated form factor and a temperature dependent Debye-Waller factor approximated with an overall thermal parameter u[23] (see supplemental materials[26] for details). We also fit simultaneously to data at all energy transfers and temperatures, for a total of nine Q and ΔE dependent data sets being fit simultaneously for each compound. For $E_i = 150$ meV and $E_i = 80$ meV, we fit data up to 8 Å^{-1}, and for $E_i = 40$ meV we fit up to 7 Å^{-1} (at which points the magnetic intensity was indistinguishable from background noise).

Using the point charge formalism described above, we fit the CEF Hamiltonians in three steps. The first step was calculating the CEF parameters for each compound using the ligand positions refined in refs.[8,9,11]. (We refer to this as the "Calculated PC" model.) As a second step, we refined the effective charges of the symmetry-

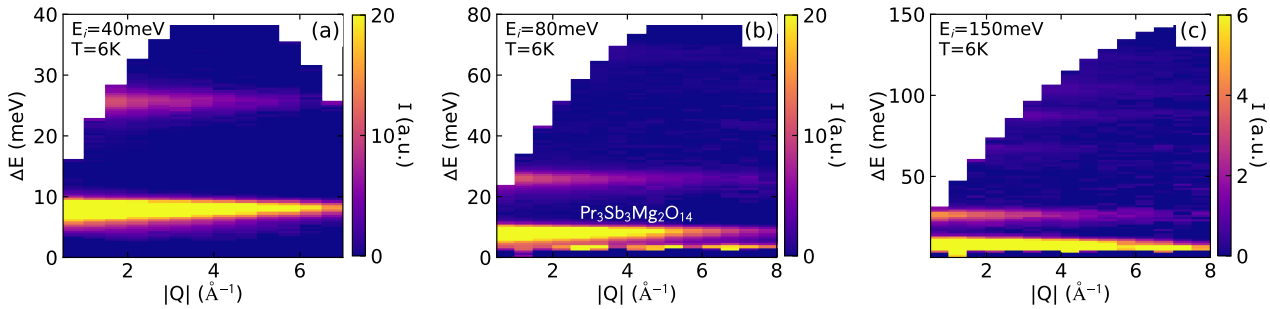

Figure 4. Inelastic neutron scattering from $Pr_3Sb_3Mg_2O_{14}$, taken at E_i =150 meV, 80 meV, and 40 meV and T =6 K (100 K and 200 K data are not shown). Scaled $La_3Sb_3Mg_2O_{14}$ scattering was subtracted. There is a very strong transition at 7.5 meV, and much weaker transitions at higher energies.

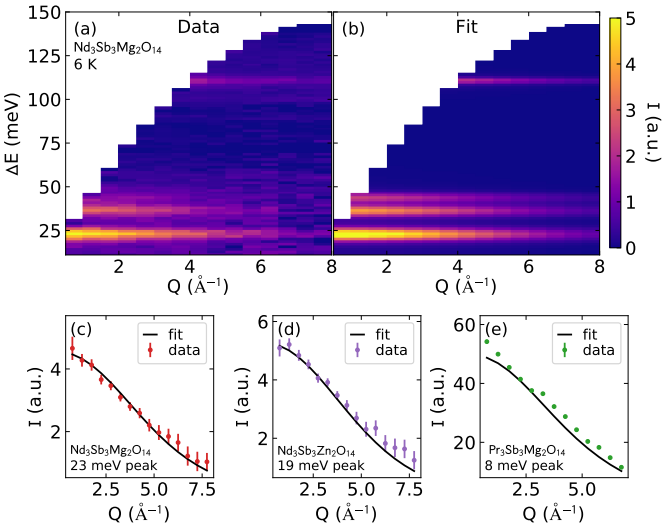

Figure 5. Example of a 2D fit to neutron scattering data. (a) and (b) show the data and final fit results of the 2D data set for $Nd_3Sb_3Mg_2O_{14}$ at 6 K. Panels (c) - (e) compare the calculated and observed Q dependence for the integrated intensity of the lowest energy excitation peaks at 6 K for the three compounds.

independent ligand sites by fitting the calculated neutron spectrum to the data. (We refer to this as the "PC Fit" model.) In $RE_3Sb_3A_2O_{14}$, there are eight ligands surrounding RE but only three symmetry-independent ligand sites. So we fit the effective charges (contained in γ_{nm}) of each symmetry-independent atom, thus fitting the relative weights of each symmetry-related group of ligands, starting with effective charges of $(-2e, -2e, -2e)$ for O^{2-} ions. By fitting effective charges, we have three fitted parameters and eight observables. In fitting the effective point charge model, we added a term to the global χ^2 measuring the mean square deviation of the calculated transitions from the observed transitions (which were taken from Gaussian fits to the spectra) of the form $\chi^2_{\Delta E} = \sum_i (E_i^{obs} - E_i^{calc})^2$. This was found to improve convergence.

As a third and final step, we used the crystal field parameters B_n^m obtained from the best effective charge fit as starting parameters for a fit to neutron data varying all B_n^m. (We refer to this as the "Final Fit" model.) We included a weakly weighted $\chi^2_{\Delta E}$ term in the final fit to keep the fit from wandering astray. In doing so, we assume that the point charge fit approaches the global minimum in χ^2 and that the final fit is merely an adjustment to the best-fit point charge model.

To cross-check our results, we computed the magnetic susceptibility from $\mathcal{H}_{CEF}$ numerically. Susceptibility is defined as $\chi_{\alpha,\beta} = \frac{\partial M_\alpha}{\partial H_\beta}$, and $M_\alpha = g_J \langle J_\alpha \rangle$, where $\langle J_\alpha \rangle = \sum_i e^{\frac{-E_i}{k_B T}} \langle i | J_\alpha | i \rangle \ / Z$ and $|i\rangle$ are the eigenstates of the effective Hamiltonian $\mathcal{H} = \mathcal{H}_{CEF} + \mu_B g_J \mu_0 \mathbf{H} \cdot \mathbf{J}$, where $\mu_0 \mathbf{H}$ is magnetic field. Computing M_α at various fields and taking a numerical derivative with respect to field yields the magnetic susceptibility. Figure 9 provides a comparison of the calculated powder-average susceptibility compared with experimental data. The calculated anistropic low-temperature magnetization is in Fig. 10.

IV. RESULTS

A. $Nd_3Sb_3Mg_2O_{14}$

The best fit CEF parameters for $Nd_3Sb_3Mg_2O_{14}$ are listed in Table I, along with the CEF parameters from the initial Calculated PC and the PC Fit models. Constant Q cuts of the fits to neutron data are shown in Fig. 6, with the final fit plotted in black and the PC fit plotted in a grey dashed line.

Starting with effective charges of $(-2e, -2e, -2e)$, the PC fitted charges for $Nd_3Sb_3Mg_2O_{14}$ are $(-0.999e, -0.931e, -0.910e)$. The Powell method of minimization[24] yields this result for any value of initial charges from $-0.6e$ to $-2e$. Although these values are about 50% less than $-2e$, they are reasonable because the electrostatic repulsion is actually from electron orbitals and not point charges; so the effective charge can differ significantly from the net charge[25]. As Fig. 6 shows, the effective charge fit resembles the data but does not reproduce the precise energies and intensities of the tran-

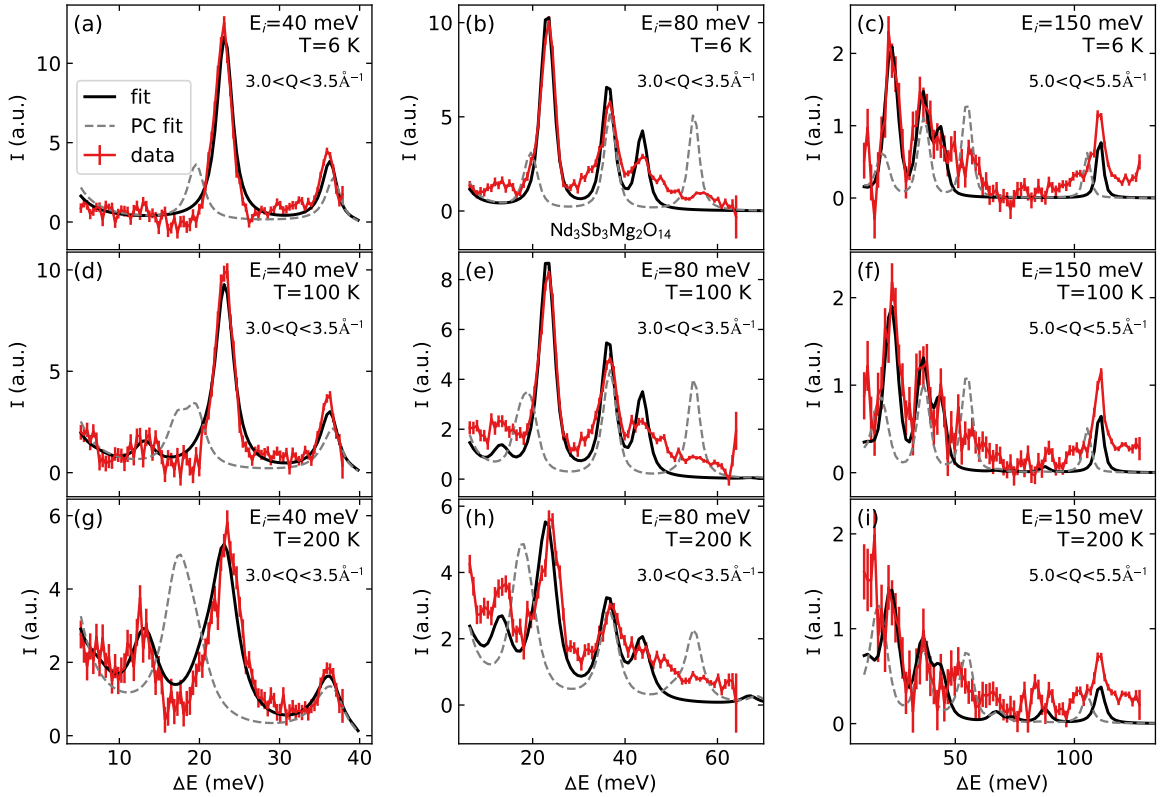

Figure 6. Constant Q cuts showing the results of the CEF fit to $Nd_3Sb_3Mg_2O_{14}$ neutron scattering data. The point charge fit ("PC fit") is shown with a grey dashed line, and the final fit ("fit") is shown with a solid black line.

Table I. Calculated and fitted CEF parameters for $Nd_3Sb_3Mg_2O_{14}$. The first column (Calculated PC) is the CEF parameters from a point-charge model where all effective charges are $2e$. The second column (PC Fit) gives the result of the effective charge fit. The final column (Final Fit) is the result of fitting the CEF parameters to the data.

B_n^m (meV)	Calculated PC	PC Fit	Final Fit
B_2^0	0.08051	-0.1851	0.0121
B_2^1	-0.5358	-0.80854	-0.25649
B_2^2	0.04892	-0.00787	-0.02649
B_4^0	-0.0131	-0.01914	-0.01861
B_4^1	0.00181	0.00297	0.00844
B_4^2	-0.00339	-0.00441	0.00763
B_4^3	-0.11134	-0.15368	-0.04106
B_4^4	0.00772	0.00994	0.0198
B_6^0	-0.00018	-0.00027	-0.00056
B_6^1	3×10^{-5}	3×10^{-5}	0.00011
B_6^2	0.00017	0.00023	-0.00028
B_6^3	0.00212	0.00293	-0.00138
B_6^4	-0.00023	-0.00031	-0.00052
B_6^5	-0.00055	-0.00081	-0.00073
B_6^6	-0.00224	-0.00309	-0.00218

sitions. The final fit matches the data much better, with the location and intensity of all major peaks reproduced.

The ground state eigenstates from the Calculated PC and the Final Fit are listed in Table II. In both fits the ground state doublet is mostly $|\pm\frac{9}{2}\rangle$, with some weight given to $|\pm\frac{3}{2}\rangle$. For the complete set of eigenkets, see the supplemental materials[26].

The ground state ordered moment, computed from $\langle 0|J_\alpha|0\rangle$ is $\langle J_x\rangle = \pm 0.11\ \mu_B$, $\langle J_y\rangle = 0.00\ \mu_B$, $\langle J_z\rangle = \mp 2.89\ \mu_B$, for a total $\langle J\rangle = \sqrt{\sum_\alpha \langle J_\alpha\rangle^2} = 2.89\ \mu_B$.

B. $Nd_3Sb_3Zn_2O_{14}$

The results of the fits to $Nd_3Sb_3Zn_2O_{14}$ data are similar to $Nd_3Sb_3Mg_2O_{14}$. Constant Q cuts of the Final Fit to $Nd_3Sb_3Zn_2O_{14}$ CEF neutron data are shown in Fig. 7. The effective charge fit (PC Fit) yielded ($-1.01e$, $-0.968e$, $-0.915e$). The PC Fit resembles the data, but the final fit matches the data much better and provides a faithful reproduction of all large peaks.

The ground state eigenkets from the final fit are listed in Table III. Like $Nd_3Sb_3Mg_2O_{14}$, the ground state doublet is mostly composed of $|\pm\frac{9}{2}\rangle$, with some $|\pm\frac{3}{2}\rangle$ also present. The initial point-charge calculation (Calculated PC) predicted significant weight on $|\pm\frac{1}{2}\rangle$ which is not present in the final fit. This indicates that the

Table II. Ground state eigenvectors and eigenvalues for $Nd_3Sb_3Mg_2O_{14}$. The top two lines give the results of the Calculated PC model, and the last two lines give the results of the Final Fit. In both cases the ground state kets are primarily $|\pm 9/2\rangle$.

Model	E (meV)	$\|-\frac{9}{2}\rangle$	$\|-\frac{7}{2}\rangle$	$\|-\frac{5}{2}\rangle$	$\|-\frac{3}{2}\rangle$	$\|-\frac{1}{2}\rangle$	$\|\frac{1}{2}\rangle$	$\|\frac{3}{2}\rangle$	$\|\frac{5}{2}\rangle$	$\|\frac{7}{2}\rangle$	$\|\frac{9}{2}\rangle$
PC calc.	0.000	0.8181	-0.0632	-0.0772	-0.1835	0.1644	0.1965	0.4597	0.0936	0.036	-0.0064
	0.000	0.0064	0.036	-0.0936	0.4597	-0.1965	0.1644	0.1835	-0.0772	0.0632	0.8181
Final Fit	0.000	0.8346	0.0211	-0.0939	-0.291	0.0711	-0.0357	0.4097	0.0782	-0.0248	0.1693
	0.000	0.1693	0.0248	0.0782	-0.4097	-0.0357	-0.0711	-0.291	0.0939	0.0211	-0.8346

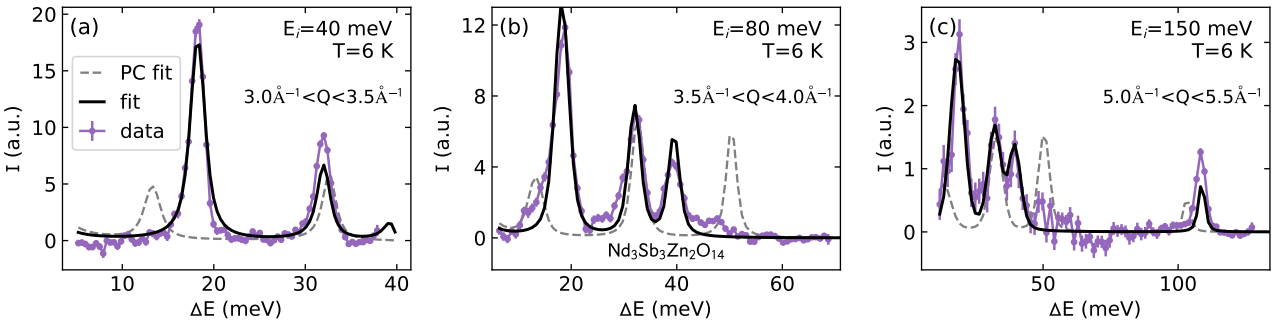

Figure 7. Constant Q cuts showing the results of the CEF fit to $Nd_3Sb_3Zn_2O_{14}$ neutron scattering data. Only $T = 6$ K data is shown; 100 K and 200 data are shown in the Supplemental Materials[26].

point-charge model, while it is a good starting point for fits, does not reliably predict the nature of the ground state doublet for these low-symmetry ligand environments. Plots of Q-cuts of higher temperature data, the list of fitted CEF parameter values, and a full list of eigenstates can be found in the supplemental materials[26].

The ground state ordered moment, computed from $\langle 0|J_\alpha|0\rangle$ is $\langle J_x\rangle = \pm 0.23\ \mu_B$, $\langle J_y\rangle = 0\ \mu_B$, $\langle J_z\rangle = \mp 2.40\,\mu_B$. The total ordered moment of $\langle J\rangle = 2.41\,\mu_B$ is slightly less than for $Nd_3Sb_3Mg_2O_{14}$.

C. $Pr_3Sb_3Mg_2O_{14}$

Constant Q cuts of the final fit to $Pr_3Sb_3Mg_2O_{14}$ CEF neutron data are shown in Fig. 8. Because Pr^{3+} is a non-Kramers ion, non-magnetic singlets are possible and there are many more energy levels and transitions. An unfortunate consequence of this is that many of the transitions are too faint to distinguish, and the neutron spectrum fit is mostly based on the low energy (< 50 meV) data. Accordingly, the $\chi^2_{\Delta E}$ term for $Pr_3Sb_3Mg_2O_{14}$ only gave significant weight to the lowest two observed energies. The PC Fit charges from the effective point charge model are ($-0.805e$ $-0.736e$, $-0.836e$). The lowest two eigenstates and eigenkets from the final fit are listed in Table IV. As required by group theory, $\langle j_x\rangle = \langle j_y\rangle = \langle j_z\rangle = 0$ for all singlet states. Plots of Q-cuts of higher temperature data, the list of fitted CEF parameter values, and a full list of eigenstates can be found in the supplemental materials[26].

The final fit resembles the data reasonably well (Fig. 8), with the exception of a predicted peak at 60 meV and too much intensity on the 85 meV peak. Nevertheless, the final fit appears to be close. We attribute the discrepancy to the fact that the high energy statistics are too weak to effectively constrain the fits to higher energy transitions, and the possible presence of orphan spins within the lattice (see below).

An alternative to directly fitting a CEF model is re-scaling the CEF parameters from a compound with a similar ligand environment. Although it is theoretically questionable for going from a Kramers ion (Nd) to a non-Kramers ion (Pr), rescaling CEF parameters has been shown to work sometimes for neighbors on the periodic table[27]. We carried out such a calculation for $Pr_3Sb_3Mg_2O_{14}$ by re-scaling the CEF parameters from the final fit B^m_n from $Nd_3Sb_3Mg_2O_{14}$ using the equation

$$\left(B^m_n\right)_{\mathrm{Pr}} = \left(B^m_n\right)_{\mathrm{Nd}} \frac{\langle r^n\rangle_{\mathrm{Pr}}\,\theta_{n\,\mathrm{Pr}}}{\langle r^n\rangle_{\mathrm{Nd}}\,\theta_{n\,\mathrm{Nd}}}, \tag{4}$$

which is derived from Eq. 2 for two different ions with the same ligand environment. While the ligand environments are not identical, this re-scaling sometimes works for two rare earth ions with similar electron counts[27]. The results are plotted in Fig. 8. Unfortunately, the re-scaled CEF parameters do not come close to predicting the energy or intensity of the transitions in the neutron spectrum. Therefore, we conclude that it is not possible to rescale the CEF parameters to accurately predict the CEF Hamiltonians of $RE_3Sb_3A_2O_{14}$.

Table III. Ground state wavefunctions for $Nd_3Sb_3Zn_2O_{14}$. The top two lines give the results from the Calculated PC model, and the last two lines give the results of the final fit. In this case, the point-charge model involves $|\pm 1/2\rangle$ while the final fit shifts most of the weight to $|\pm 9/2\rangle$.

Model	E (meV)	$\|-\frac{9}{2}\rangle$	$\|-\frac{7}{2}\rangle$	$\|-\frac{5}{2}\rangle$	$\|-\frac{3}{2}\rangle$	$\|-\frac{1}{2}\rangle$	$\|\frac{1}{2}\rangle$	$\|\frac{3}{2}\rangle$	$\|\frac{5}{2}\rangle$	$\|\frac{7}{2}\rangle$	$\|\frac{9}{2}\rangle$
PC calc.	0.000	0.4198	-0.0573	-0.2189	0.1273	-0.4703	-0.5831	0.4015	0.1527	0.1031	0.0
	0.000	0.0	-0.1031	0.1527	-0.4015	-0.5831	0.4703	0.1273	0.2189	-0.0573	-0.4198
Final Fit	0.000	0.2368	0.0265	0.0455	0.4932	0.0389	0.0939	0.1583	0.0049	-0.0336	0.8133
	0.000	0.8133	0.0336	0.0049	-0.1583	0.0939	-0.0389	0.4932	-0.0455	0.0265	-0.2368

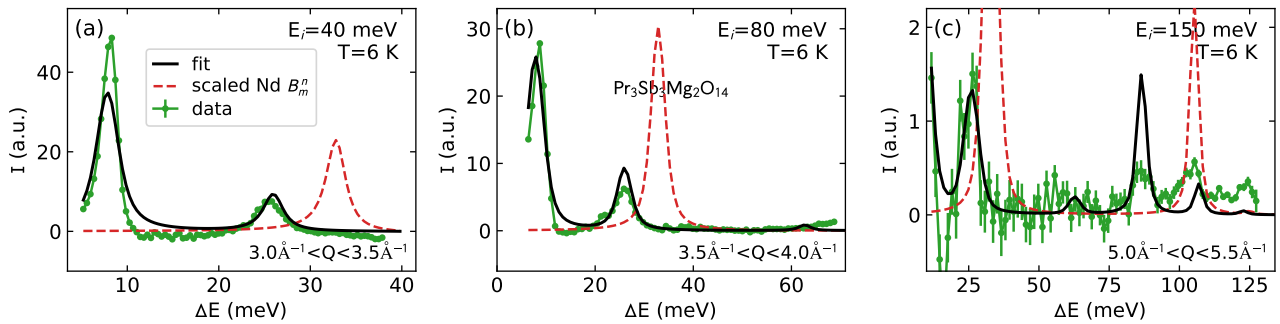

Figure 8. Constant Q cuts showing the results of the final fit to $Pr_3Sb_3Mg_2O_{14}$ neutron scattering data, along with the results of rescaling the CEF parameters from $Nd_3Sb_3Mg_2O_{14}$. Only $T = 6$ K data are shown; 100 K and 200 data are shown in the Supplemental Materials[26]. Clearly, the rescaled CEF parameters are unreliable. The black fit line is not as good as for the Nd compounds, especially for the higher energy transitions in panel (c).

D. Susceptibility

The calculated magnetic susceptibilities for all three compounds based on the final fit CEF Hamiltonians are plotted in Fig. 9, along with experimental data from refs.[8,9,11]. In every case, the χ_{CEF} calculation (plotted with a gray dashed line) overestimates the measured susceptibility by about 10% (the predicted inverse susceptibility curve lies below the data). The reason for this discrepancy appears to be impurities or site-mixing in the compounds, mainly evidenced by the low-temperature $Pr_3Sb_3Mg_2O_{14}$ data.

In the $Pr_3Sb_3Mg_2O_{14}$ experimental susceptibility plotted in Fig. 9(c), $\chi^{-1} \to 0$ as $T \to 0$. This should not happen for a singlet ground state (non-Kramers ion in a low-symmetry ligand field), where χ should saturate at a finite value. The deviation to zero indicates Kramers ions in the sample. To estimate the relative contribution, we fit the $Pr_3Sb_3Mg_2O_{14}$ susceptibility to a simple model: $\chi = (x)\chi_{CEF} + (1-x)\chi_{CW}$, where $0 < x < 1$ and χ_{CW} is represented by a Curie-Weiss law: $\frac{C}{T-\theta_C}$. The fit works surprisingly well, and indicates a 13% orphan spin contribution with an effective moment of 1.8 μ_B (see Supplemental Materials[26] for more details). Such a contribution could arise from site mixing between Pr and Mg, like the $\sim$ 10% Dy/Mg site mixing observed in $Dy_3Sb_3Mg_2O_{14}$[12]. This would decouple some of the spins from the kagome planes, and put them in completely different ligand environments. However, we were unable to identify any site

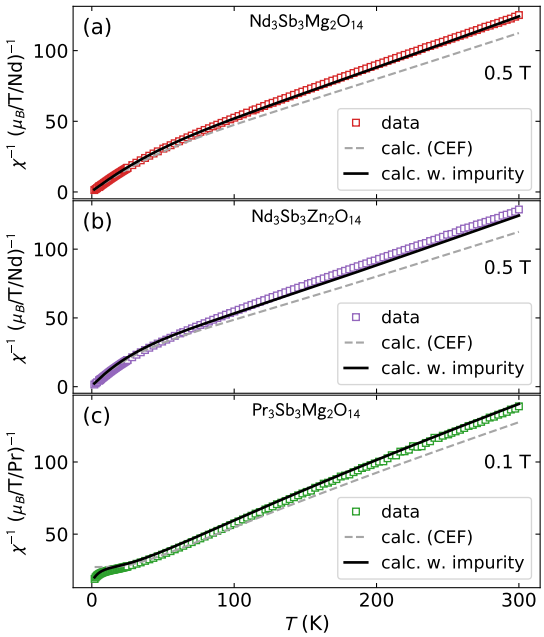

Figure 9. Comparison between the measured susceptibility and the susceptibility calculated from the final fit CEF Hamiltonians. In each case the calculation overestimates the high temperature susceptibility by about 10%, which may result from chemical impurities in the samples used for susceptibility measurements.

Table IV. Eigenvectors and eigenvalues for the ground state and first excited crystal field state of $Pr_3Sb_3Mg_2O_{14}$. The top two lines give the results of the calculated PC model, and the last two lines give the results of the final fit. As a non-Kramers ion, the ground state is not constrained to be a doublet. As required for singlets, $\langle j_x \rangle = \langle j_y \rangle = \langle j_z \rangle = 0$ for all states.

Model	E (meV)	$\|-4\rangle$	$\|-3\rangle$	$\|-2\rangle$	$\|-1\rangle$	$\|0\rangle$	$\|1\rangle$	$\|2\rangle$	$\|3\rangle$	$\|4\rangle$
PC calc.	0.000	0.0211	0.1351	0.0143	0.0677	-0.9762	-0.0677	0.0143	-0.1351	0.0211
	9.028	0.481	-0.0515	-0.0064	-0.5137	-0.0648	0.5137	-0.0064	0.0515	0.481
Final Fit	0.000	0.2851	-0.1002	0.2334	0.3867	-0.6398	-0.3867	0.2334	0.1002	0.2851
	7.963	-0.1683	-0.0653	0.0903	-0.4922	-0.6587	0.4922	0.0903	0.0653	-0.1683

mixing in structural refinements, so we cannot positively identify site-mixing as the cause. Alternatively, these orphan ions may be from second phases or other RE ions mixed in with Pr. The experiments in this study are not sufficient to determine the orphan spins? origin.

We also attempted to account for the susceptibility discrepancy using an interaction model $\chi = \frac{\chi_{CEF}}{1-\lambda\chi_{CEF}}$ where λ is the magnetic interaction between ions. No matter what λ is chosen, model fails to account for the low temperature divergence, and it fails to correct the slope of high temperature susceptibility. Thus, the observed effects indicate an additional Cure-Weiss contribution to the susceptibility and not merely interactions.

Incorporating this Curie-Weiss contribution model makes the calculations match the low-temperature $Pr_3Sb_3Mg_2O_{14}$ susceptibility data well, and happens to resolve the high-temperature discrepancy between theory and experiment. Assuming that the Nd^{3+} compounds have the same χ_{CW}, we also get good agreement between theory and experiment for $Nd_3Sb_3Mg_2O_{14}$ and $Nd_3Sb_3Zn_2O_{14}$ (Fig. 9).

We tested and ultimately rejected three alternative explanations for the high-temperature discrepancy between calculated and measured susceptibility: (i) an incorrect CEF Hamiltonian, (ii) sample diamagnetism and (iii) higher multiplet mixing. We tested (i) by attempting to re-fit the CEF Hamiltonian to the neutron data including a χ^2 term from calculated susceptibility (without χ_{CW}). This attempt failed. No matter what starting parameters are chosen (and the relative χ^2 weight given to susceptibility versus neutron spectrum), we were unable to fit them simultaneously. We tested (ii) by measuring the susceptibility of the non-magnetic analogue $La_3Sb_3Mg_2O_{14}$, which comes out to -10^{-4} (μ_B/T/ion)—an order of magnitude too small. We tested (iii) by calculating susceptibility using the intermediate coupling-scheme and found that the result is nearly identical to the fits based on the Hunds rule spin-orbital ground state. (Details behind (ii) and (iii) are given in the Supplemental Materials[26], which includes Ref.[28,29].) Therefore, we are confident that the discrepancy between calculated and measured susceptibility in $Pr_3Sb_3Mg_2O_{14}$ is due to orphan Kramers ions in the sample.

The presence of orphan spins may explain some of the slight discrepancies in the neutron spectrum. However, 10% population of orphan spins is too little to significantly affect the CEF excitation spectrum, and the statistics in the high-energy $Pr_3Sb_3Mg_2O_{14}$ are simply too low to identify and fit peaks of an impurity signal. Nevertheless, the presence of such spins may be enough to have effects on some forms of collective phenomena in these frustrated magnets.

V. DISCUSSION

The point-charge fit followed by the final CEF parameter fit seems to have worked as a method to determine the crystal field level scheme in the low point group symmetry $RE_3Sb_3A_2O_{14}$ compounds. The final fit matches the data well, and along the way the fitted effective charges are within an electron charge from the formal ligand charge. Furthermore the calculated temperature dependent susceptibility reproduces measurements well after accounting for orphan spins at the <10% level. We are confident that we have identified the single-ion CEF Hamiltonians for $Nd_3Sb_3Mg_2O_{14}$, $Nd_3Sb_3Zn_2O_{14}$, and $Pr_3Sb_3Mg_2O_{14}$ and determined the associated crystal field eigenvalues and eigenstates.

The analysis of $Nd_3Sb_3Zn_2O_{14}$ shows that the point-charge model by itself does not reliably predict the ground state eigenkets of $RE_3Sb_3A_2O_{14}$ compounds. Here we note that we are basing the models on a high T x-ray structural refinement. Low T neutron diffraction measurements would provide more accurate ligand positions, which could improve the point charge fitting. We find that scaling Nd^{3+} results to Pr^{3+} does not reproduce the observed spectrum in $Pr_3Sb_3Mg_2O_{14}$. Therefore, it is unfortunately not possible to accurately predict the CEF ground states of other $RE_3Sb_3A_2O_{14}$ compounds from these results.

For Pr^{3+} the lowest level states of the single-ion non-Kramers states are singlets. This is true for the naive calculated PC Hamiltonian, the PC fit Hamiltonian, and the final fit Hamiltonian. The gap between the lowest and first excited state exceeds the exchange energy scale so that we expect this system to be a singlet ground state system with no phase transitions.

One of the key features of interest for these compounds is the magnetic anisotropy. One can gain a rough understanding of the single ion anisotropy by examining

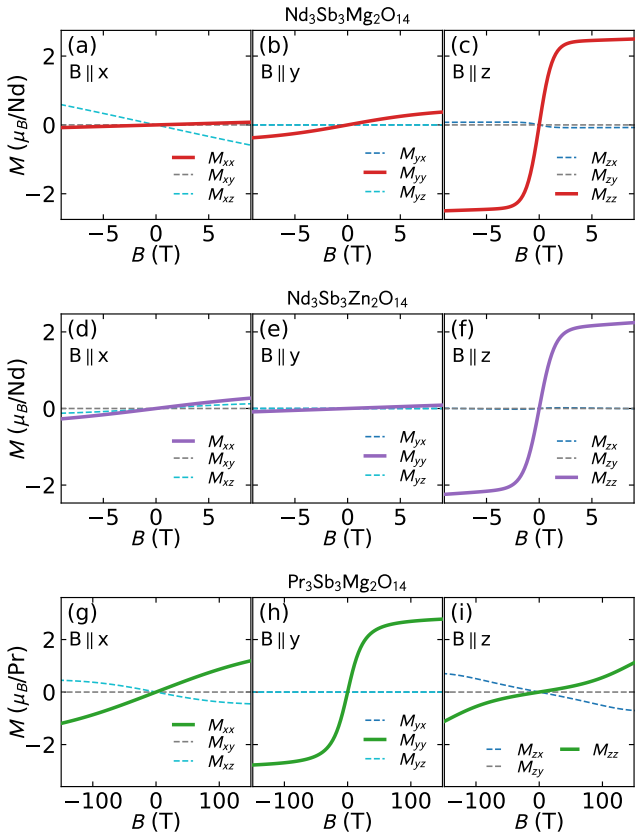

Figure 10. Directional single ion magnetization computed from the final fit CEF Hamiltonians for $Nd_3Sb_3Mg_2O_{14}$, $Nd_3Sb_3Zn_2O_{14}$, and $Pr_3Sb_3Mg_2O_{14}$ at 2 K. The directions x, y, and z are defined in Fig. 1.

the ground state wave function. The final fit results for $Nd_3Sb_3Mg_2O_{14}$ and $Nd_3Sb_3Zn_2O_{14}$ have mostly an effective $J = |\pm\frac{9}{2}\rangle$ ground state doublet, which can be interpreted as easy-axis moments. The substitution of Zn for Mg does not have a dramatic effect on the ground state, at least for the Nd^{3+} ion. For a clearer picture of the anisotropy, the computed single-ion directional magnetization at 2 K is shown in Fig. 10. For $Nd_3Sb_3Mg_2O_{14}$ and $Nd_3Sb_3Zn_2O_{14}$, the saturation magnetic field is around 5 T, with the largest magnetization for $B \parallel z$, indicating an easy-axis. In both compounds, negligibly small off-diagonal zx and xz elements are present. For $Pr_3Sb_3Mg_2O_{14}$, the predicted saturation magnetic field is around 80 T with the easiest axis in the y direction.

These results show that the authors' previously hypothesized effective $J = |\pm\frac{1}{2}\rangle$ Nd^{3+} ground state for $Nd_3Sb_3Mg_2O_{14}$[11] is incorrect, and Dun et. al.'s suggestion of an easy axis[10] is closer to the true ground state. Ref.[11] failed to account for impurities in magnetization, which led to the inference of an incorrect model.

The ordered moment in $Nd_3Sb_3Mg_2O_{14}$ determined from neutron scattering is $1.79(5)\,\mu_B$[11]. Assuming a 13% site-mixing, this is only 71% of the theoretically predicted moment of $(0.87 \times 2.89\,\mu_B) = 2.51\,\mu_B$. This reduction in moment, in conjunction with the magnetic entropy not reaching $R\ln(2)$[11], suggests that the magnetism in $Nd_3Sb_3Mg_2O_{14}$ remains dynamic to the lowest temperatures. This suggests a closer examination of the collective properties of this material in a high quality single crystal sample would be interesting.

VI. CONCLUSION

We have outlined a method whereby complex inelastic neutron scattering spectra for crystal field excitations of rare earth ions can be fitted using a point-charge model with effective ligand charges as an intermediate step. We applied this method to Nd^{3+} in $Nd_3Sb_3Mg_2O_{14}$ and $Nd_3Sb_3Zn_2O_{14}$, showing that the single-ion anisotropy is easy-axis. We also applied the method to Pr^{3+}, showing that the ground state is a singlet with an energy gap of 8.0 meV.

This information is an essential component towards understanding the low-temperature magnetism of this new family of frustrated magnets, and will guide further investigations of their collective properties.

Note: While this manuscript was in the final stages of preparation, there appeared Ref.[30] which independently implemented an effective point charge fit to the CEF Hamiltonian of $Ho_3Sb_3Mg_2O_{14}$.

ACKNOWLEDGMENTS

This work was supported through the Institute for Quantum Matter at Johns Hopkins University, by the U.S. Department of Energy, Division of Basic Energy Sciences, Grant DE-FG02-08ER46544. AS and CB were supported through the Gordon and Betty Moore foundation under the EPIQS program GBMF4532. ADC was partially supported by the U.S. DOE, Office of Science, Basic Energy Sciences, Materials Sciences and Engineering Division. This research at the High Flux Isotope Reactor and Spallation Neutron Source was supported by DOE Office of Science User Facilities Division. AS acknowledges helpful discussions with Andrew Boothroyd.

[1] K. Essafi, O. Benton, and L. D. C. Jaubert, Nature Communications **7**, 10297 EP (2016).

[2] R. R. P. Singh and D. A. Huse, Phys. Rev. Lett. **68**, 1766 (1992).

[3] S. Yan, D. A. Huse, and S. R. White, Science **332**, 1173 (2011).

[4] S.-S. Gong, W. Zhu, L. Balents, and D. N. Sheng, Phys. Rev. B **91**, 075112 (2015).

[5] M. Hirschberger, R. Chisnell, Y. S. Lee, and N. P. Ong, Phys. Rev. Lett. **115**, 106603 (2015).

[6] K. Ohgushi, S. Murakami, and N. Nagaosa, Phys. Rev. B **62**, R6065 (2000).

[7] Z. L. Dun, J. Trinh, K. Li, M. Lee, K. W. Chen, R. Baumbach, Y. F. Hu, Y. X. Wang, E. S. Choi, B. S. Shastry, A. P. Ramirez, and H. D. Zhou, Phys. Rev. Lett. **116**, 157201 (2016).

[8] M. B. Sanders, K. M. Baroudi, J. W. Krizan, O. A. Mukadam, and R. J. Cava, physica status solidi (b) **253**, 2056 (2016).

[9] M. B. Sanders, J. W. Krizan, and R. J. Cava, J. Mater. Chem. C **4**, 541 (2016).

[10] Z. L. Dun, J. Trinh, M. Lee, E. S. Choi, K. Li, Y. F. Hu, Y. X. Wang, N. Blanc, A. P. Ramirez, and H. D. Zhou, Phys. Rev. B **95**, 104439 (2017).

[11] A. Scheie, M. Sanders, J. Krizan, Y. Qiu, R. J. Cava, and C. Broholm, Phys. Rev. B **93**, 180407 (2016).

[12] J. A. Paddison, H. S. Ong, J. O. Hamp, P. Mukherjee, X. Bai, M. G. Tucker, N. P. Butch, C. Castelnovo, M. Mourigal, and S. Dutton, Nature communications **7**, 13842 (2016).

[13] Z.-F. Ding, Y.-X. Yang, J. Zhang, C. Tan, Z.-H. Zhu, and L. Chen, Gang Shu, ArXiv (2018).

[14] A. Abragam and B. Bleaney, *Electron Paramagnetic Resonance of Transition Ions*, 1st ed. (Clarendon Press, Oxford, 1970).

[15] A. Scheie, "Pycrystalfield," `https://github.com/asche1/PyCrystalField` (2018).

[16] K. W. H. Stevens, Proceedings of the Physical Society. Section A **65**, 209 (1952).

[17] M. Hutchings, Solid State Physics, **16**, 227 (1964).

[18] J. Mesot and A. Furrer, "The crystal field as a local probe in rare earth based high-temperature superconductors," in *Neutron Scattering in Layered Copper-Oxide Superconductors*, edited by A. Furrer (Springer Netherlands, Dordrecht, 1998) pp. 335–374.

[19] U. Walter, Journal of Physics and Chemistry of Solids **45**, 401 (1984).

[20] S. Edvardsson and M. Klintenberg, Journal of Alloys and Compounds **275-277**, 230 (1998).

[21] A. Furrer, J. Mesot, and T. Strässle, *Neutron scattering in condensed matter physics* (World Scientific, 2009).

[22] D. L. Abernathy, M. B. Stone, M. J. Loguillo, M. S. Lucas, O. Delaire, X. Tang, J. Y. Y. Lin, and B. Fultz, Review of Scientific Instruments **83**, 015114 (2012).

[23] G. L. Squires, *Introduction to the Theory of Thermal Neutron Scattering* (Cambridge University Press, 1978).

[24] M. J. D. Powell, The Computer Journal **7**, 155 (1964).

[25] D. Newman and B. Ng, *Crystal Field Handbook* (Cambridge University Press, 2007).

[26] See Supplemental Material at [URL will be inserted by publisher] for more details of the experimental and computational methods.

[27] W. T. Carnall, G. L. Goodman, K. Rajnak, and R. S. Rana, The Journal of Chemical Physics **90**, 3443 (1989).

[28] S. P. Tandon and P. C. Mehta, The Journal of Chemical Physics **52**, 4896 (1970).

[29] J. Rodriguez-Carvajal, Physica B: Condensed Matter **192**, 55 (1993).

[30] Z. Dun, X. Bai, J. A. Paddison, N. P. Butch, C. D. Cruz, M. B. Stone, T. Hong, M. Mourigal, and H. Zhou, arXiv preprint arXiv:1806.04081 (2018).